

Article

Numerical Study of Cattaneo–Christov Heat Flux on Water-Based Carreau Fluid Flow over an Inclined Shrinking Sheet with Ternary Nanoparticles

Sanju Jangid ¹, Nazek Alessa ^{2,*} , Ruchika Mehta ^{1,*}, N. Thamarai Kannan ³  and Shilpa ¹ Department of Mathematics & Statistics, Manipal University Jaipur, Jaipur 303007, Rajasthan, India² Department of Mathematical Sciences, College of Sciences, Princess Nourah Bint Abdulrahman University, P.O. Box 84428, Riyadh 11671, Saudi Arabia³ Department of Mathematics, Erode Arts and Science College, Erode 638009, Tamilnadu, India

* Correspondence: nazekaa@yahoo.com (N.A.); ruchika.mehta@jaipur.manipal.edu (R.M.)

Abstract: Due to their capacity to create better thermal conductivity than standard nanofluids, hybrid nano-fluids and modified nanofluids have notable applications in aerospace, energy materials, thermal sensors, antifouling, etc. This study aims to the modified and hybrid nanofluid flow with the Carreau fluid over a sloped shrinking sheet. The Cattaneo–Christov heat flux also takes into account. To determine the thermal efficiency of the heat, three different kinds of nanomaterials, copper oxide (CuO), copper (Cu), and alumina (Al_2O_3), are used. The similarity alteration commutes the insolubility of the model into ODEs. The conclusions are attained by program writing in MATLAB software and dealing with them through the bvp4c solver with the shooting method. The skin-friction amount decreases with the inclined sheet and local Weissenberg parameter for both modified and hybrid nanofluid. An upsurge thermal relaxation parameter declines the skin-friction coefficient for modified nanofluid flow and increases the skin-friction coefficient for hybrid nanofluid flow. The heat transfer rate is upsurged with modified and hybrid nanofluid for thermal relaxation parameter. Furthermore, the presentation includes the development of skin friction coefficient and Nusselt number values for specific parameters. Through benchmarking, numerical solutions are validated using certain limiting situations that were previously published findings, and typically solid correlation is shown.

Keywords: Carreau fluid; modified nanoparticles; Cattaneo–Christov heat flux; inclined shrinking sheet; bvp4c solver



Citation: Jangid, S.; Alessa, N.; Mehta, R.; Thamarai Kannan, N.; S. Numerical Study of Cattaneo–Christov Heat Flux on Water-Based Carreau Fluid Flow over an Inclined Shrinking Sheet with Ternary Nanoparticles. *Symmetry* **2022**, *14*, 2605. <https://doi.org/10.3390/sym14122605>

Academic Editors: Mikhail Sheremet and Abderrahmane Bairi

Received: 20 October 2022

Accepted: 2 December 2022

Published: 8 December 2022

Publisher's Note: MDPI stays neutral with regard to jurisdictional claims in published maps and institutional affiliations.



Copyright: © 2022 by the authors. Licensee MDPI, Basel, Switzerland. This article is an open access article distributed under the terms and conditions of the Creative Commons Attribution (CC BY) license (<https://creativecommons.org/licenses/by/4.0/>).

1. Introduction

Researchers have expressed great interest in studying non-Newtonian fluids because of their numerous uses. The abundance of these fluids in nature is the fundamental cause of this. Non-Newtonian performance is also used in services like lubrication and biomedical flows and in mining, where slurries and mud are frequently curbed. The significance of modeling non-Newtonian fluid flow phenomena for the industry is evident. There has been a significant amount of research in non-Newtonian fluids, but many more studies are required in non-Newtonian fluid models. Many researchers have studied the power-law model to look into non-Newtonian effects because of its relative simplicity. The power-law model, however, has some drawbacks. Here, we consider the Carreau fluid model, another viscous model, due to the shortcomings of the power-law model, particularly at meager and high shear rates. The Carreau viscosity model helps designate the flow performance of fluids in the high shear rate section. Shear thickening (dilatant) and shear thinning (pseudo-plastic) fluid characteristics are defined by the Carreau fluid, a subdivision of the non-Newtonian fluid model.

Additionally, Fourier's law indicated the heat transmission mechanism in 1822. The idea that the medium under examination instantly recognizes the actual temperature is

based on this law. To remedy this issue, Cattaneo introduced a thermal relaxation period to Fourier's law. This phrase describes the time a medium need to transport heat to the surrounding particles. Christov also enhanced this model. The heat flux model of Cattaneo–Christov is the new model (C-C) name. Ref. [1] discussed the phase dissemination dynamics using a sand column with a changing water table in a capillary fringe. Ref. [2] discussed the MHD power-law fluid flow with prescribed heat flux along with the heat source/sink and the power-law-dependent thermal conductivity over an extending permeable surface. Ref. [3] studied the time-independent 2D stagnation point fluid flow and heat transference to a melting extending/reduction sheet. The viscous dissipation and heat conductivity were analyzed by [4] with the unvarying temperature and unvarying heat flux for improved power law fluids moving between the equivalent plates with single plate stirring. Ref. [5] inspected the peristaltic Carreau fluid flow in a porous rectangular channel. The wall shear stress delivery was studied by [6] in six-well culture plates with planar orbital transformation. Ref. [7] deliberated the 2D Carreau fluid flow passes through a porous extending sheet along with convective boundary circumstance. Ref. [8] researched the melting phenomenon on the time-independent mixed convective flow about a vertical surface fixed in a porous [9] medium. Ref. [10] investigated for coupled flow and heat transmission of an upper convective Maxwell fluid above an extending plate along with velocity slip impact. Ref. [11] deal with nanofluids mixed convective heat transmission past a concentric erect annulus. Ref. [12] deliberated the blood flow or Carreau fluid over a tapering artery with stenosis. Ref. [13] discussed the Blasius and Sakiadis flow of Carreau fluid along with the Deborah number. Ref. [14] inspected the 2D MHD Powell–Eyring fluid flow over an extending sheet. Ref. [9] discussed the Cattaneo–Christov heat flux of the spinning viscoelastic fluid flow over a spreading surface. The heat transmission to a Carreau fluid flow over a nonlinear extending surface was inspected by [15]. Ref. [16] presented an MHD Carreau fluid flow over a convective energized surface in the company of nonlinear thermal radiation. Ref. [17] discussed the Cattaneo–Christov theory and thermal conductivity (depending on temperature) of Jeffrey fluid over a non-linear stretchy surface along with inconstant width and stagnation point flow.

Other applications of magnetohydrodynamic (MHD) viscous incompressible flow of electrically conducting fluid include processing magnetic materials, managing heat transfer, removing impurities from crude oil, Hall generators, etc. Such flows result in the generation of a Lorentzian magnetic body force that is transverse to the direction of the applied magnetic field and helps control energy flux, dampen oscillations, and high-temperature plasmas. Colloidal suspensions of magnetizable nanoparticles with magnetic, fluid, and thermal characteristics make up magnetic nanofluids. Ref. [18] explored the mixed-convective heat transmission of water-Cu nanofluids privileged a 90° angle curvature microtube. Ref. [19] explored the time-dependent convective micropolar fluid flow with Soret, reaction rate, and radiation impacts passing through an upright porous surface with dynamic viscidness (depending on temperature) and unvarying vortex viscidness. Ref. [20] analyzed the 3D forced convective Carreau fluid flow over a bi-directional strained surface. Ref. [21] studied the 2D hydromagnetic Carreau fluid flow passes an inconstant extending sheet. Ref. [22] discussed comparing $Cu - Al_2O_3$ /water hybrid nanofluid and Cu /water nanofluid flows past an extending sheet. Ref. [23] explored the non-Fourier heat flux influence on the stagnation-point Carreau fluid flow. Ref. [24] presented the dual explanations of a Carreau fluid flow over a non-linear slopped reduction surface in the company of immeasurable shear rate viscidness. A time-dependent hydromagnetic natural convective flow with radiative impact and reaction rate impact passes through a porous erect plate explored by [25]. Ref. [26] studied the entropy production impression on hydro-magnetic hybrid nanofluid (Al_2O_3-Cu/H_2O) flow because of the porous stretching sheet with inconstant heat flux in the presence of the electric field. Ref. [27] studied a Slippage impact on peristaltic transport hydromagnetic Jeffery hybrid nanofluid (TiO_2-Cu/H_2O) in an asymmetric channel with viscous dissipation and Hall current impressions.

With their low heat resistance and effective thermo-physical characteristics, nanofluids have become one of the most desirable areas of study. Further, maintaining the intended performance of several industrial and the cooling of technical devices, including computers, laptops, power electronics, motors, and high-powered rays, is essential. Results showed a 23.8% improvement at 0.1% solid copper nanoparticle volume fraction-Their greater surface area and thermal conductivity suit copper nanoparticles to this growth. We spoke about more than fifty distinct nanofluids made of water, ethylene glycol, and motor oil with SiO_2 , Al_2O_3 , TiO_2 , ZrO_2 , and diamond particles. The range of solid nanoparticles was 0.25 to 8%, with particle sizes restricted to 10 to 150 nm. The classical theory does not specify thermal conductivity for nanofluids. A few analyses have been developed for two types of particles floating in a base fluid called a hybrid nanofluid. To create a hybrid nanofluid, two different kinds of solid nanoparticles have been dispersed throughout the base fluid in several experimental and computational studies. The next generation of nanofluids is hybrid nanofluids, and the next generation of hybrid nanofluids is modified nanofluids. Ref. [28] discussed the thermal features of the ternary hybrid nanomaterials ($\text{CuO} - \text{Cu} - \text{Al}_2\text{O}_3$) between two equivalent walls with entropy creation and nonlinear thermal radiation. Ref. [29] focused on hydromagnetic Carreau nanofluid flow over a paraboloid surface along with the Cattaneo–Christov heat flux. Ref. [30] inspected the entropy creation of radiative Carreau fluid flow in a slopped microchannel in viscous heating. Ref. [31] examined the radiative flow of Oldroyd-B liquid induced by a stretchy sheet with cross diffusion and chemical reaction effects. Ref. [32] analyzed the Xue model and Yamada–Ota model hybrid nanofluid flow with a slopped magnetic field over a dynamic cylinder. Refs. [33,34] discussed a 2D hydromagnetic SWCNTs or MWCNTs/saline water nanofluid flow with mixed convection above an extending/shrinking plate with a melting effect.

Here, we concentrate on copper, aluminium oxide, and copper oxide as the three most common nanoparticles. Due to their thermal solid and chemical durability, antimicrobial capabilities, and antibacterial characteristics, aluminium oxide nanoparticles are an excellent choice for water treatment. Al_2O_3 nanoparticles also exhibit properties useful in biological applications such as medication delivery, biofiltration, and sensors. Significant anti-bacterial properties of copper make it helpful in treating infectious epidemics. It is a well-established antibacterial and antifungal agent. The radiative Fe_3O_4 , MoS_2 - H_2O hybrid nanofluid flow was inspected by [35] over a slopped plate with ascent heating and heat source/sink impressions. A study on the second law analysis and mixed convective rheology of the (Al_2O_3 - $\text{Ag} / \text{H}_2\text{O}$) hybrid nanofluid flow influenced by magnetic induction properties to a stretching sheet with viscous dissipation and internal heat generation effects studied by [36]. Ref. [37] investigated the thermal radiation and non-uniform heat flux influences on MHD hybrid nanofluid ($\text{CuO} - \text{Fe}_2\text{O}_3 / \text{H}_2\text{O}$) flow along a stretching cylinder with velocity slip condition. Ref. [38] studied the heat transmission of an engine oil-based fluid flow at an inclination of 45° to the plane. Ref. [39] focused on the inclined plate solar collector substituted by the hybrid nanofluid holding MgO , CuO with MWCNTs and water. Ref. [40] explored the ternary nanofluid flow at a non-linear extending Riga plate with variable viscidness. Ref. [41] studied the unsteady 3D water-driven hybrid nanofluid with the consequences of brick-shaped nanocomposites (ceria and zinc oxide) with the thermal link of heat source/sink and variable thermal conditions within the magnetic environment. Ref. [42] investigated the flow of the glycerin-based carbon nanotubes with velocity slip in Darcy–Forchheimer porous medium on a convectively heated Riga plate along with the Cattaneo–Christov theory. Ref. [43] inspected the thermal conductivity, Cattaneo–Christov heat flux, and activation energy in 2D incompressible nanofluid flow with base fluid water over a curved extending sheet looped in a round using the Koo–Kleinstreuer–Li model.

Heat transmission is one of the fundamental and most significant phenomena in several engineering and manufacturing fields. The function of heat transmission is communicated by several technical and manufacturing developments, including extrusion operations, electronic chilling, the refining sector, and premium heated oil. Fluids considered to be in a nano-size configuration are called nanofluids. These liquids blend base

liquids and nanoparticles, such as carbon nanotubes or carbides, oxides, and metals (including glycol, ethylene, oil, water, etc.). The creation of semiconductor materials, crystal growth, welding processes, the glass industry, material sanitization, and many other industrial processes have significantly benefited from the research of melting phenomena in recent years. The variable viscosity (depending on temperature) and thermal conductivity were explored by [44] with modified Fourier's law in a fluid flow with tiny materials over a revolving disk. Ref. [45] inspected the modified Fourier heat flux influence of MHD radiative nanofluid flow privileged a hole occupied with ethylene glycol-multiwalled carbon nanotubes. Ref. [46] discussed the study of the convective flow of Cross fluid ($Al_2O_3 - Cu/CMC$) containing carboxymethyl cellulose water over a stretching sheet with convective heating. Ref. [47] studied the hydromagnetic mixed convective flow of CNTs nanofluid in water past a heated stretchy plate with injection/suction, heat consumption, viscous dissipation, and radiation. Ref. [48] examined the bi-directional Williamson fluid flow in a porous extending sheet along with the thermophoresis, Brownian motion, zero mass flux, and modified Darcy's law. The hydromagnetic stagnation point flow of Al_2O_3 /water nanofluid over a reduction sheet and viscous dissipation, melting, and Ohmic heating impressions were elucidated by [49]. Ref. [50] explicated the MoO_2-Co /sodium alginate-based hybrid nanofluid flow with the ramped motion of a limitless inclined plate. Ref. [51] deliberated entropy production investigation for a peristaltic flow in a rotating medium with generalized compliant walls.

The primary goal of this paper is to analyze the performance of a Carreau-modified nanofluid flowing over a surface that is inclined and shrinking in the context of the Cattaneo–Christov heat flux. Till now, nobody studied the Carreau-modified nanofluid flow in the presence of the Cattaneo–Christov heat flux over an inclined shrinking surface. The three different forms of modified nanoparticles—copper oxide (CuO), copper nanoparticles (Cu), and aluminium oxide (Al_2O_3)—are used to examine the thermal deal. By using the bvp4c approach along with the shooting technique, the simulated problem solution is calculated. The behavior of the relevant impressions has been investigated through diagrams and tables. Additionally, the findings of earlier analyses by Wahid et al. [49] and Bachok et al. Ref. [3] have been compared with those of the present investigation. We expect the current study to assist other future researchers by using several flow models and varied geometries.

2. Mathematical Design

The next are the situations and managerial ethics that govern the current model given in Figure 1:

- 2D hydromagnetic time-independent stagnation-point flow
- Carreau modified nanofluid flow with CuO , Cu , and Al_2O_3 nanoparticles
- Inclined shrinking sheet
- Cattaneo–Christov heat flux
- The motion of the reduction sheet is $u_w(x)$, and the movement of the inviscid flow is $u_e(x)$, The melting temperature is T_m and the free stream temperature T_∞ .

The suitable Navier–Stoke's equations that control the flow conventions are the equation of continuity, velocity, and energy, which were obtained by (Wahid et al. [49] and Bachok et al. [3], Ahmad and Pop [8], Devi and Devi [22]):

Equation of continuity:

$$\frac{\partial u}{\partial x} + \frac{\partial v}{\partial y} = 0 \quad (1)$$

Equation of motion:

$$\begin{aligned} & \rho_{mnf} \left(u \frac{\partial u}{\partial x} + v \frac{\partial u}{\partial y} \right) \\ &= \rho_{mnf} u_e \frac{du_e}{dx} + \mu_{mnf} \left(\frac{\partial^2 u}{\partial y^2} \right) \left(1 + \Gamma^2 \left(\frac{\partial u}{\partial y} \right)^2 \right)^{(n-1)/2} + \mu_{mnf} (n \\ & - 1) \Gamma^2 \left(\frac{\partial^2 u}{\partial y^2} \right) \left(\frac{\partial u}{\partial y} \right)^2 \left(1 + \Gamma^2 \left(\frac{\partial u}{\partial y} \right)^2 \right)^{(n-3)/2} - \sigma_{mnf} B_0^2 (u \\ & - u_e) + g (\rho \beta_T)_{mnf} \cos \alpha (T - T_m) \end{aligned} \tag{2}$$

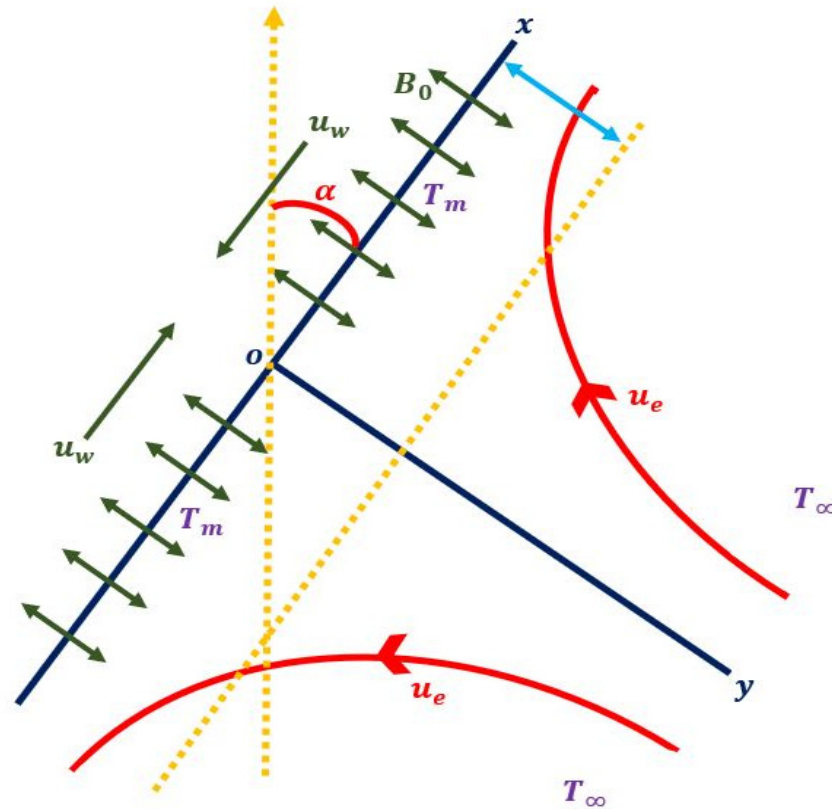


Figure 1. Flow chart of current problem.

Equation of temperature:

$$\begin{aligned} & (\rho C_p)_{mnf} \left[u \frac{\partial T}{\partial x} + v \frac{\partial T}{\partial y} \right. \\ & \left. + \lambda_T \left\{ \left(u \frac{\partial u}{\partial x} + v \frac{\partial u}{\partial y} \right) \frac{\partial T}{\partial x} + \left(u \frac{\partial v}{\partial x} + v \frac{\partial v}{\partial y} \right) \frac{\partial T}{\partial y} + u^2 \frac{\partial^2 T}{\partial x^2} \right. \right. \\ & \left. \left. + v^2 \frac{\partial^2 T}{\partial y^2} + 2uv \frac{\partial^2 T}{\partial x \partial y} \right\} \right] \\ &= k_{mnf} \frac{\partial^2 T}{\partial y^2} + \sigma_{mnf} B_0^2 (u - u_e)^2 + \mu_{mnf} \left(\frac{\partial u}{\partial y} \right)^2 \end{aligned} \tag{3}$$

The boundary circumstances for the existing case are as tracks (Jumana et al. [34]):

$$\begin{aligned} & u = u_w(x); T = T_m; \frac{k_{mnf}}{\rho_{mnf}} \left(\frac{\partial T}{\partial y} \right) = (L + C_s(T_m - T_0)) v(x); \text{ at } y = 0 \\ & u \rightarrow u_e(x); T \rightarrow T_\infty; \text{ at } y \rightarrow \infty \end{aligned} \tag{4}$$

The components of motion in the coordinates of y and x are denoted by v (meter/second-m/s) and u (meter/second-m/s), respectively, $u_w(x) = cx$ and $u_e(x) = ax$ with a and c are the constants, C_s standing for the solid surface specific heat, L stands for the latent heat, T_0 depicts the solid surface temperature, T_m depicts the melting point temperature, acute angle (α) , λ_T is the thermal relaxation constants, the heat that is transmitted to

the melting surface is equivalent to the sum of the sensible energy mandatory to get the temperature T_0 up to the melting point and the melting heat temperature at a point T_m , T (Kelvin-K) is the fluid temperature and Γ is the time constant. Furthermore, mnf stands for modified nanofluid, $hbnf$ stands for hybrid nanofluid, $(\rho C_p)_{mnf}$ signifies the heat capacity of the modified nanofluid, B_0 (Tesla-T) shows the strength of the magnetic field, the gravitational acceleration is g , σ_{mnf} depicts the electrical conductivity, $(\rho\beta_T)_{mnf}$ stands for the thermal expansion coefficient, k_{mnf} signifies the thermal conductivity of the modified nanofluid, ρ_{mnf} symbolizes the density of the modified nanofluid, and μ_{mnf} denotes the modified nanofluid dynamic viscosity. Remember that the Newtonian situation is signified by the power law index $n = 1$ in Equation (2). Naturally, a power law index value between 0 and 1 characterizes the shear thinning behavior of fluids, whereas $n > 1$ results in the shear thickening behavior. Table 1 shows the formulas for topographies of nanoparticles.

Table 1. The methods and boundaries for the modified and hybrid nanofluid in the scheme above equations are (Abbasi et al. [28]):

Thermal Properties	Modified Nanofluid	Hybrid Nanofluid
Thermal Diffusivity	$\alpha_{Tmnf} = \frac{k_{mnf}}{(\rho C_p)_{mnf}}$	$\alpha_{Thbnf} = \frac{k_{hbnf}}{(\rho C_p)_{hbnf}}$
Viscosity	$\frac{\mu_{mnf}}{\mu_{Bf}} = \frac{1}{(1-\phi_{CuO})^{2.5}(1-\phi_{Cu})^{2.5}(1-\phi_{Al_2O_3})^{2.5}}$	$\frac{\mu_{hbnf}}{\mu_{Bf}} = \frac{1}{(1-\phi_{Cu})^{2.5}(1-\phi_{CuO})^{2.5}}$
Heat Capacity	$\frac{(\rho C_p)_{mnf}}{(\rho C_p)_{Bf}} = (1-\phi_{Al_2O_3})((1-\phi_{Cu})((1-\phi_{CuO}) + \phi_{CuO} \frac{(\rho C_p)_{CuO}}{(\rho C_p)_{Bf}}) + \phi_{Cu} \frac{(\rho C_p)_{Cu}}{(\rho C_p)_{Bf}} + \phi_{Al_2O_3} \frac{(\rho C_p)_{Al_2O_3}}{(\rho C_p)_{Bf}}$	$\frac{(\rho C_p)_{hbnf}}{(\rho C_p)_{Bf}} = \phi_{Cu} \frac{(\rho C_p)_{Cu}}{(\rho C_p)_{Bf}} + (1-\phi_{Cu}) \left((1-\phi_{CuO}) + \phi_{CuO} \frac{(\rho C_p)_{CuO}}{(\rho C_p)_{Bf}} \right)$
Density	$\frac{(\rho)_{mnf}}{(\rho)_{Bf}} = (1-\phi_{Al_2O_3}) \left((1-\phi_{Cu})((1-\phi_{CuO}) + \phi_{CuO} \frac{(\rho)_{CuO}}{(\rho)_{Bf}}) + \phi_{Cu} \frac{(\rho)_{Cu}}{(\rho)_{Bf}} + \phi_{Al_2O_3} \frac{(\rho)_{Al_2O_3}}{(\rho)_{Bf}} \right)$	$\frac{(\rho)_{hbnf}}{(\rho)_{Bf}} = \phi_{Cu} \frac{(\rho)_{Cu}}{(\rho)_{Bf}} + (1-\phi_{Cu}) \left((1-\phi_{CuO}) + \phi_{CuO} \frac{(\rho)_{CuO}}{(\rho)_{Bf}} \right)$
Thermal expansion	$\frac{(\rho\beta_T)_{mnf}}{(\rho\beta_T)_{Bf}} = (1-\phi_{Al_2O_3}) \left((1-\phi_{Cu})((1-\phi_{CuO}) + \phi_{CuO} \frac{(\rho\beta_T)_{CuO}}{(\rho\beta_T)_{Bf}}) + \phi_{Cu} \frac{(\rho\beta_T)_{Cu}}{(\rho\beta_T)_{Bf}} + \phi_{Al_2O_3} \frac{(\rho\beta_T)_{Al_2O_3}}{(\rho\beta_T)_{Bf}} \right)$	$\frac{(\rho\beta_T)_{hbnf}}{(\rho\beta_T)_{Bf}} = \phi_{Cu} \frac{(\rho\beta_T)_{Cu}}{(\rho\beta_T)_{Bf}} + (1-\phi_{Cu}) \left((1-\phi_{CuO}) + \phi_{CuO} \frac{(\rho\beta_T)_{CuO}}{(\rho\beta_T)_{Bf}} \right)$
Thermal Conductivity	$k_{mnf} = \frac{k_{CuO} + (M-1)k_{Bf} - (M-1)\phi_{CuO}(k_{Bf} - k_{CuO})}{k_{CuO} + (M-1)k_{Bf} + \phi_{CuO}(k_{Bf} - k_{CuO})} k_{Bf}$ $k_{hbnf} = \frac{k_{Cu} + (M-1)k_{Bf} - (M-1)\phi_{Cu}(k_{Bf} - k_{Cu})}{k_{Cu} + (M-1)k_{Bf} + \phi_{Cu}(k_{Bf} - k_{Cu})} k_{Bf}$ $k_{mnf} = \frac{k_{Al_2O_3} + (M-1)k_{hbnf} - (M-1)\phi_{Al_2O_3}(k_{hbnf} - k_{Al_2O_3})}{k_{Al_2O_3} + (M-1)k_{hbnf} + \phi_{Al_2O_3}(k_{hbnf} - k_{Al_2O_3})} k_{hbnf}$	$k_{hbnf} = \frac{k_{Cu} + (M-1)k_{Bf} - (M-1)\phi_{Cu}(k_{Bf} - k_{Cu})}{k_{Cu} + (M-1)k_{Bf} + \phi_{Cu}(k_{Bf} - k_{Cu})} k_{Bf}$ $k_{mnf} = \frac{k_{CuO} + (M-1)k_{Bf} - (M-1)\phi_{CuO}(k_{Bf} - k_{CuO})}{k_{CuO} + (M-1)k_{Bf} + \phi_{CuO}(k_{Bf} - k_{CuO})} k_{Bf}$
Electrical Conductivity	$\sigma_{mnf} = \frac{\sigma_{CuO} + (M-1)\sigma_{Bf} - (M-1)\phi_{CuO}(\sigma_{Bf} - \sigma_{CuO})}{\sigma_{CuO} + (M-1)\sigma_{Bf} + \phi_{CuO}(\sigma_{Bf} - \sigma_{CuO})} \sigma_{Bf}$ $\sigma_{hbnf} = \frac{\sigma_{Cu} + (M-1)\sigma_{Bf} - (M-1)\phi_{Cu}(\sigma_{Bf} - \sigma_{Cu})}{\sigma_{Cu} + (M-1)\sigma_{Bf} + \phi_{Cu}(\sigma_{Bf} - \sigma_{Cu})} \sigma_{Bf}$ $\sigma_{mnf} = \frac{\sigma_{Al_2O_3} + (M-1)\sigma_{hbnf} - (M-1)\phi_{Al_2O_3}(\sigma_{hbnf} - \sigma_{Al_2O_3})}{\sigma_{Al_2O_3} + (M-1)\sigma_{hbnf} + \phi_{Al_2O_3}(\sigma_{hbnf} - \sigma_{Al_2O_3})} \sigma_{hbnf}$	$\sigma_{mnf} = \frac{\sigma_{CuO} + (M-1)\sigma_{Bf} - (M-1)\phi_{CuO}(\sigma_{Bf} - \sigma_{CuO})}{\sigma_{CuO} + (M-1)\sigma_{Bf} + \phi_{CuO}(\sigma_{Bf} - \sigma_{CuO})} \sigma_{Bf}$ $\sigma_{hbnf} = \frac{\sigma_{Cu} + (M-1)\sigma_{Bf} - (M-1)\phi_{Cu}(\sigma_{Bf} - \sigma_{Cu})}{\sigma_{Cu} + (M-1)\sigma_{Bf} + \phi_{Cu}(\sigma_{Bf} - \sigma_{Cu})} \sigma_{Bf}$

where C_p is the specific heat at constant pressure, ϕ_{CuO} represents the volume fraction of CuO , ϕ_{Cu} describes the volume fraction of Cu , $\phi_{Al_2O_3}$ describes the volume fraction of Al_2O_3 , and k_{Bf} , μ_{Bf} , ρ_{Bf} and σ_{Bf} represent the thermal conductivity, dynamic viscosity, density, and electrical conductivity of the regular fluid, respectively. The subscripts Bf , $hbnf$, mnf , CuO , Cu , and Al_2O_3 symbolize the base fluid, modified nanofluid, hybrid

nanofluid, copper oxide, copper, and aluminum oxide nanoparticles, respectively. As an outcome, Table 1 covers data from the working fluid and three different nanomaterials CuO , Cu , and Al_2O_3 . The physical properties of nanofluids are given in Table 2.

Table 2. Physical properties of $CuO - Cu - Al_2O_3$ /water hybrid nanoparticles (Abbasi et al. [28]):

Physical Characteristics	Water	CuO	Cu	Al_2O_3
ρ	997.1	6320	8933	3970
C_p	4179	531.8	385	765
k	0.613	76.5	401	40
σ	5.5×10^{-6}	6.9×10^{-2}	59.6×10^6	35×10^6
β_T	21	1.80	1.67	0.85
Pr	6.2	-	-	-

In the existing circumstances, we may clarify our investigation by holding the next non-dimensional quantities (Jumana et al. [34]):

$$\eta = \sqrt{\frac{a}{\nu_{Bf}}}y, \quad v = -\sqrt{av_{Bf}}f, \quad u = axf', \quad \theta(\eta) = \frac{T - T_m}{T_\infty - T_m} \tag{5}$$

In Equations (1) and (4), the changed ODEs and boundary conditions are obtained by rearranging (6) to (8) as:

$$\frac{\mu_{mnf}/\mu_{Bf}}{\rho_{mnf}/\rho_{Bf}}(1 + nW^2 f''^2) \left(1 + W^2 f''^2\right)^{(n-3)/2} f''' + ff'' + 1 + f'^2 - \frac{\sigma_{mnf}/\sigma_{Bf}}{\rho_{mnf}/\rho_{Bf}} Mn(f' - 1) + \frac{(\rho\beta_T)_{mnf}/(\rho\beta_T)_{Bf}}{\rho_{mnf}/\rho_{Bf}} \cos\alpha G_T\theta = 0. \tag{6}$$

$$\frac{1}{Pr} \left(\frac{k_{mnf}/k_{Bf}}{(\rho C_p)_{mnf}/(\rho C_p)_{Bf}} - \delta_T f^2 \right) \theta'' + f\theta' - \delta_T f f' \theta' + \frac{\mu_{mnf}/\mu_{Bf}}{(\rho C_p)_{mnf}/(\rho C_p)_{Bf}} Ec f''^2 + \frac{\sigma_{mnf}/\sigma_{Bf}}{(\rho C_p)_{mnf}/(\rho C_p)_{Bf}} Ec Mn(f' - 1)^2 = 0 \tag{7}$$

With the boundary situations in issue

$$f(0) + \frac{Me}{Pr} \frac{k_{Bf}}{(\rho)_{mnf}} \theta'(0) = 0, \quad f'(0) = \lambda, \quad \theta(0) = 0 \quad \text{at } \eta = 0 \tag{8}$$

$$f'(\infty) \rightarrow 1, \quad \theta(\infty) \rightarrow 1 \quad \text{at } \eta \rightarrow \infty$$

The local Weissenberg number (W), Hartmann parameter (Mn), local Grashof temperature number (G_T), Prandtl effect (Pr), thermal relaxation parameter (δ_T) Eckert number (Ec), Stretching/Shrinking parameter (λ), and Melting parameter (Me) are all parameters utilized to designate the nondimensional amounts in Equations (6) to (8). The constant shrinking parameter is $\lambda = \frac{c}{a} < 0$, while the static sheet is represented by $\lambda = 0$. These quantities are specified by formula as

$$W = \Gamma \sqrt{\frac{xa^3}{\nu_{Bf}}} \Gamma, \quad Mn = \frac{\sigma_{Bf} B_0^2}{\rho_{Bf} a}, \quad G_T = \frac{g(\beta_T)_{Bf}(T_\infty - T_m)}{a^2 x}, \quad Pr = \frac{\nu_{Bf}}{\alpha_{Bf}}, \quad \delta_T = \lambda_T a Ec = \frac{a^2 x^2}{(C_p)_{Bf}(T_\infty - T_m)},$$

and $Me = \frac{(C_p)_{Bf}(T_\infty - T_m)}{L + C_s(T_\infty - T_m)}$, and $\lambda = c/a$.

We note that the Stefan numbers $(C_p)_{Bf}(T_\infty - T_m)/L$ and $C_s(T_\infty - T_m)/L$ for the base fluid and solid surface, respectively, are combined to form the melting parameter Me .

The shear stress and heat transfer rate are physical amounts of practical engineering concern, and they are explained as tracks:

The skin friction is $C_f = \frac{\tau_w}{\rho_{Bf} u_e^2}$, and the Nusselt number is $Nu_x = \frac{xq_w}{k_{Bf}(T_\infty - T_m)}$.

The surface shear stress τ_w is supposed by $\tau_w = \mu_{mnf} \left(\frac{\partial u}{\partial y} \left(1 + \frac{\Gamma}{\sqrt{2}} \frac{\partial u}{\partial y} \right) \right)_{y=0}$, we get

$$C_{fx} Re_x^{1/2} = \mu_{mnf} / \mu_{Bf} [f''(0) + (W/2)(f''(0))^2],$$

The rate of heat transfer q_w is supposed by $q_w = -k_{hbnf} \left(\frac{\partial T}{\partial y} \right)_{y=0}$ (here negative sign shows that the temperature is reducing from higher to lower.), we get

$$Nu_x Re_x^{-1/2} = -\left(k_{mnf} / k_{Bf} \right) \theta'(0),$$

where, $Re_x = \frac{u_e(x)}{v_{Bf}}$ is the Reynolds number.

3. Numerical Structure

Equations are resolved through the bvp4c solver. All numerical amounts and diagrams are established with MATLAB, which is debated in the tables and graphs. Let

$$f = y(1), \quad f' = y(2), \quad f'' = y(3), \quad \theta = y(4), \quad \theta' = y(5).$$

Equations (6) to (8) reduce into newform as follows:

$$\begin{aligned} & \frac{\mu_{mnf} / \mu_{Bf}}{\rho_{mnf} / \rho_{Bf}} (1 + nW^2 y(3)^2) (1 + W^2 y(3)^2)^{(n-3)/2} f''' + y(1)y(3) + 1 + y(1)^2 \\ & - \frac{\sigma_{mnf} / \sigma_{Bf}}{\rho_{mnf} / \rho_{Bf}} Mn(y(1) - 1) + \frac{(\rho\beta_T)_{mnf} / (\rho\beta_T)_{Bf}}{\rho_{mnf} / \rho_{Bf}} \cos\alpha G_T y(4) \\ & = 0 \end{aligned}$$

$$\begin{aligned} & \frac{1}{Pr} \left(\frac{k_{mnf} / k_{Bf}}{(\rho C_p)_{mnf} / (\rho C_p)_{Bf}} - \delta_T y(1)^2 \theta'' + y(1)y(5) - \delta_T y(1)y(2)y(5) \right. \\ & \left. + \frac{\mu_{mnf} / \mu_{Bf}}{(\rho C_p)_{hbnf} / (\rho C_p)_{Bf}} Ecy(3)^2 \right. \\ & \left. + \frac{\sigma_{mnf} / \sigma_{Bf}}{(\rho C_p)_{hbnf} / (\rho C_p)_{Bf}} EcMn(y(2) - 1)^2 = 0 \right. \end{aligned}$$

With the boundary conditions in issue:

$$\begin{aligned} y_0(1) + \frac{Me}{Pr} \frac{\frac{k_{mnf}}{k_{Bf}}}{\frac{(\rho)_{mnf}}{(\rho)_{Bf}}} y_0(5) &= 0, & y_0(2) &= \lambda, & y_0(4) &= 0 & \text{at } \eta = 0 \\ y_\infty(2) &\rightarrow 1, & y_\infty(4) &\rightarrow 1 & & & \text{at } \eta \rightarrow \infty \end{aligned}$$

The choice $\eta(\infty) = 5$ or 7 designates that each numerical outcome accesses asymptotic assets ideally in this method.

4. Code Verification

Justification of existing conclusions is proved in current research. Table 3 endows a juxtaposition of the known research consistencies. However, highly accurate outcomes for the present investigation are searched.

Table 3. Assessment regarding the amounts of $f''(0)$ (at $\lambda = 2$) and $-\theta'(0)$ (at $\lambda = 1$) with Me , when $Pr = 1$, and non-appearance of further rest numbers.

Me	$f''(0)$ at $\lambda=2$			Me	$-\theta'(0)$ at $\lambda=1$		
	Bachok et al. [3]	Wahid et al. [49]	Current Work		Bachok et al. [3]	Wahid et al. [49]	Current Work
0	-1.8873066	-1.887306668	-1.887306668	0	-0.7978846	-0.797884573	-0.797884573
1	-1.5804839	-1.580483902	-1.580483902	1	-0.5060545	-0.506054476	-0.506054476
2	-1.4427473	-1.442747275	-1.442747275	2	-0.3826383	-0.382638279	-0.382638279
3	-1.3592105	-1.359210504	-1.359210504	3	-0.3119564	-0.311956405	-0.311956405

5. Result and Discussion

The properties of separate water-based nanofluid, notably CuO , Cu , and Al_2O_3 /water (spherical shape), are assessed utilizing a *bvp4c* solver. The implications of developing flow features are enumerated utilizing a variety of produced graphs and tables. Figures 2–12 and Tables 4 and 5 exhibit the interactions of various physical factors on the amounts of the Nusselt, skin friction, temperature, and velocity obtained using MATLAB programming. According to our measurements, the physical factors for the present study are as follows: $Pr = 6.2$, $\alpha = \frac{\pi}{4}$, $\phi_{CuO} = 0.20$, $\phi_{Cu} = 0.25$, $\phi_{Al_2O_3} = 0.35$, $\delta_T = 0.001$, $W = Mn = GT = n = Me = Ec = 0.1$, and $\lambda = -0.1$.

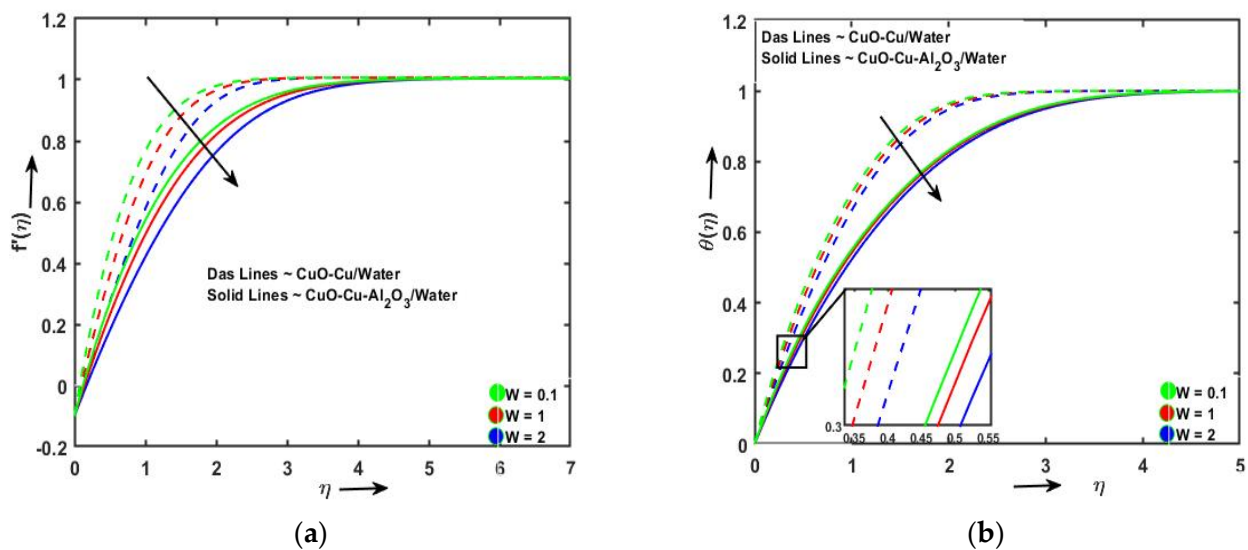


Figure 2. The (a) momentum and (b) temperature profiles of Weissenberg parameter W .

Figure 2a, Figure 3a, and Figure 4a depict the falling momentum profiles of the growing Weissenberg parameter, acute angle, and local Grashof temperature number, respectively. The fluid velocity toward the Weissenberg number is shown in Figure 2a. It is detected that with an upsurge Weissenberg number, the motion outline declines because the growing amounts of the Weissenberg number bring improvement in the relaxation time of the fluid particles, and hence viscosity occurs more prominent, which makes resistance to the fluid flow; as an outcome, the fluid motion declines.

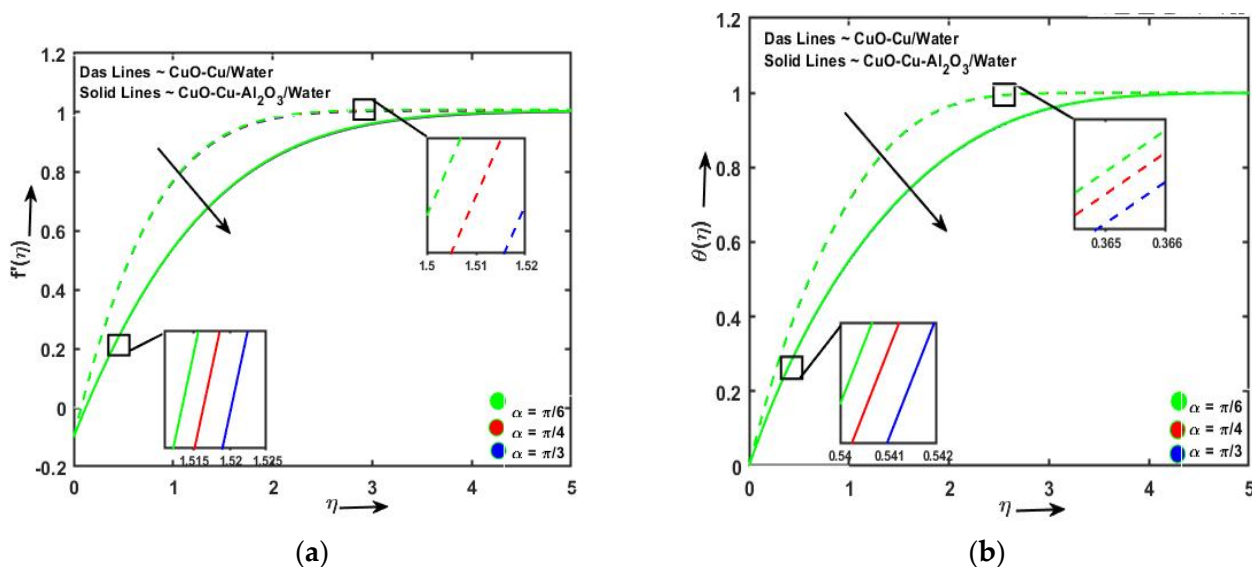


Figure 3. The (a) momentum and (b) temperature profiles of acute angle α .

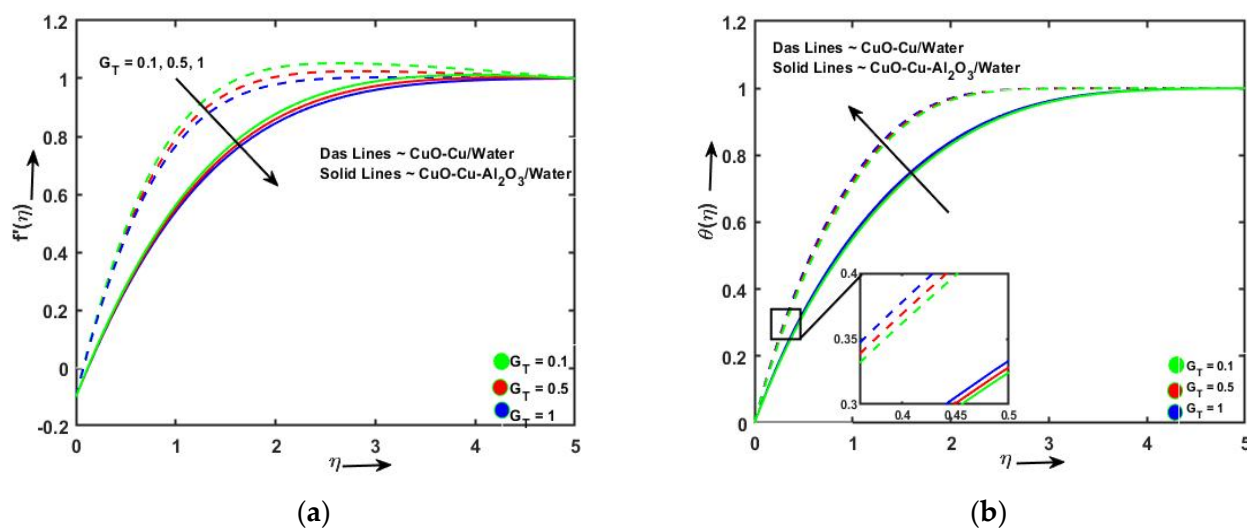


Figure 4. The (a) momentum and (b) temperature profiles of local temperature Grashof parameter G_T .

In detail, Figure 3a shows the effect of an inclination towards fluid motion. It is observed that there is an opposite connection between an inclination and motion outline; for significant amounts of an inclination, the motion diagram falloffs. When we upsurge an inclination about the x-axis, the impact of gravity falls, which fetches a failure in fluid motion within a boundary layer. The upsurge in local temperature Grashof number declines the velocity profile (Figure 4a) because of the decrease in the thickness of the momentum boundary layer. Figures 2b and 3b depict the declining temperature profiles of the growing Weissenberg parameter and an acute angle, respectively. Figure 4b displays the increasing influence of the temperature of the Grashof number due to the upsurge thickness of the thermal boundary layer for both modified and hybrid nanofluid.

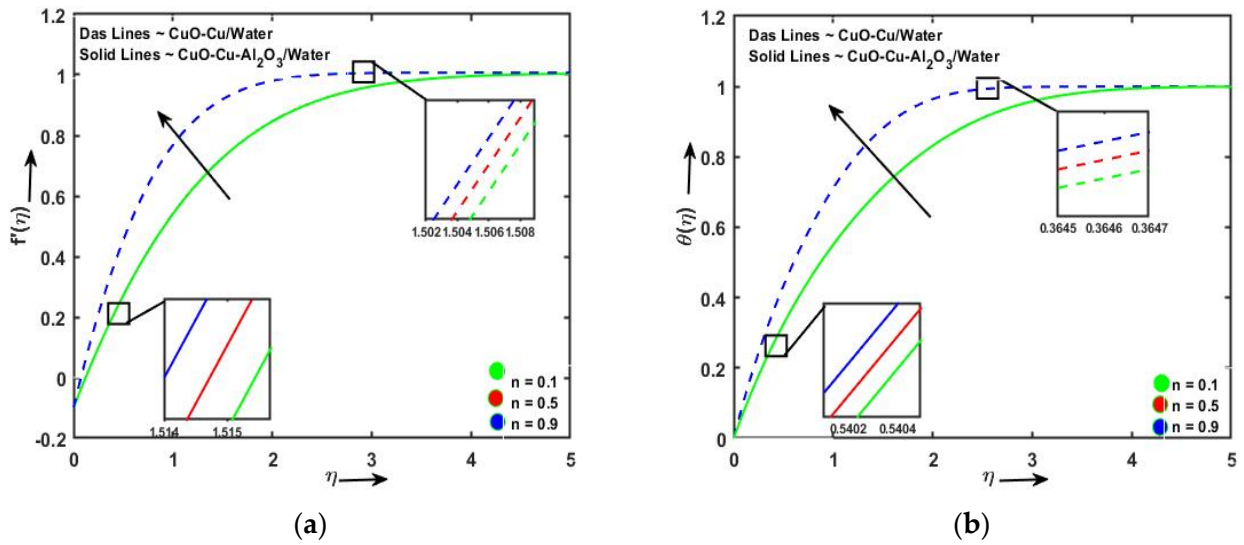


Figure 5. The (a) momentum and (b) temperature profiles of power law index n .

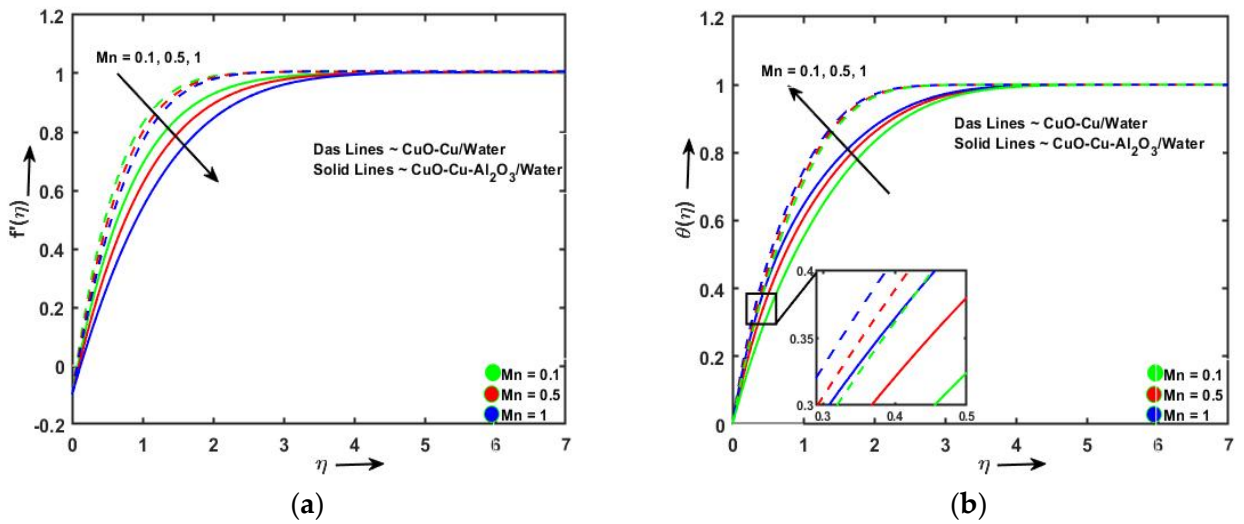


Figure 6. The (a) momentum and (b) temperature profiles of magnetic parameter Mn .

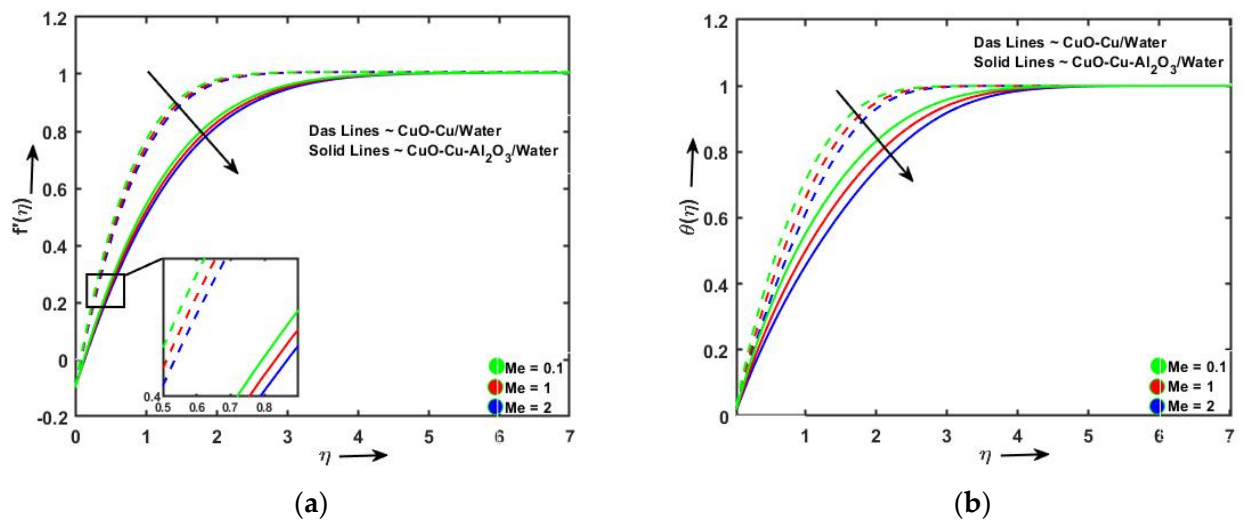


Figure 7. The (a) momentum and (b) temperature profiles of melting parameter Me .

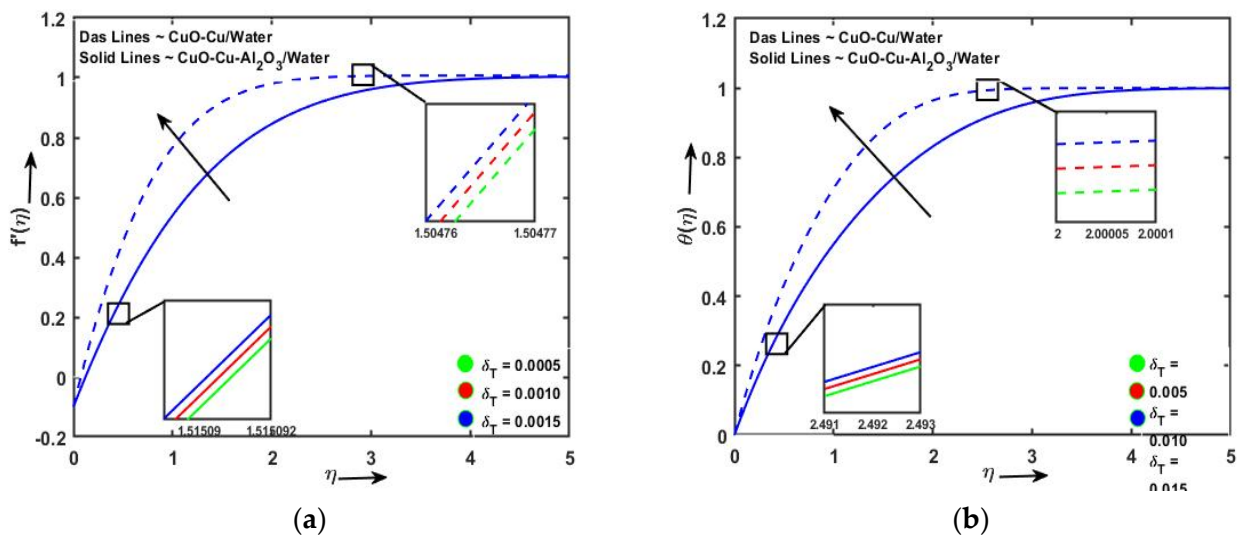


Figure 8. The (a) momentum and (b) temperature profiles of thermal relaxation parameter δ_T .

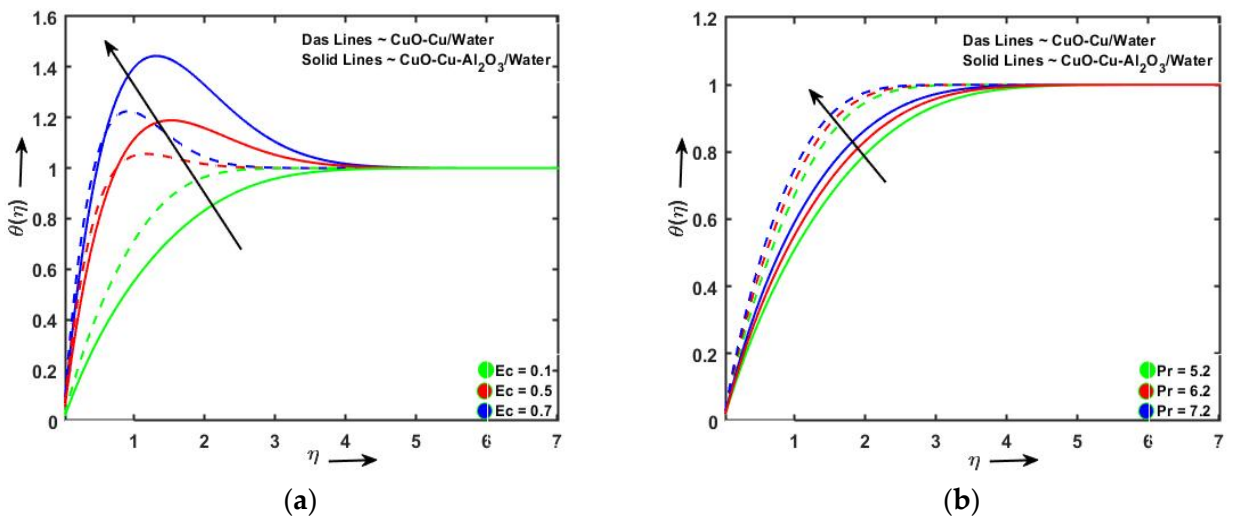


Figure 9. The temperature profiles of (a) Eckert parameter Ec and (b) Prandtl number Pr .

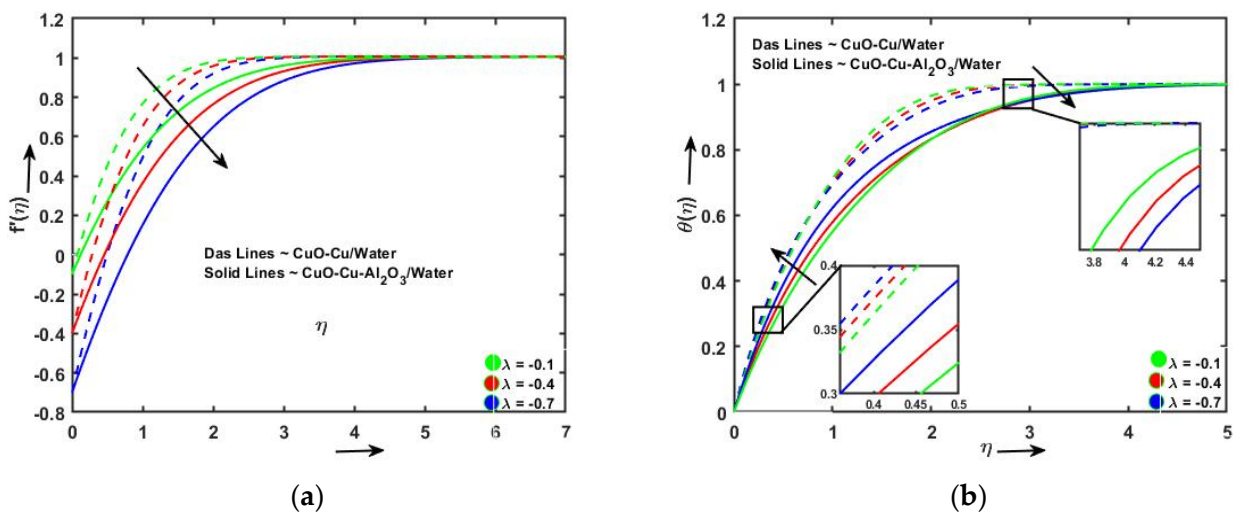


Figure 10. The (a) momentum and (b) temperature profiles of shrinking parameter λ .

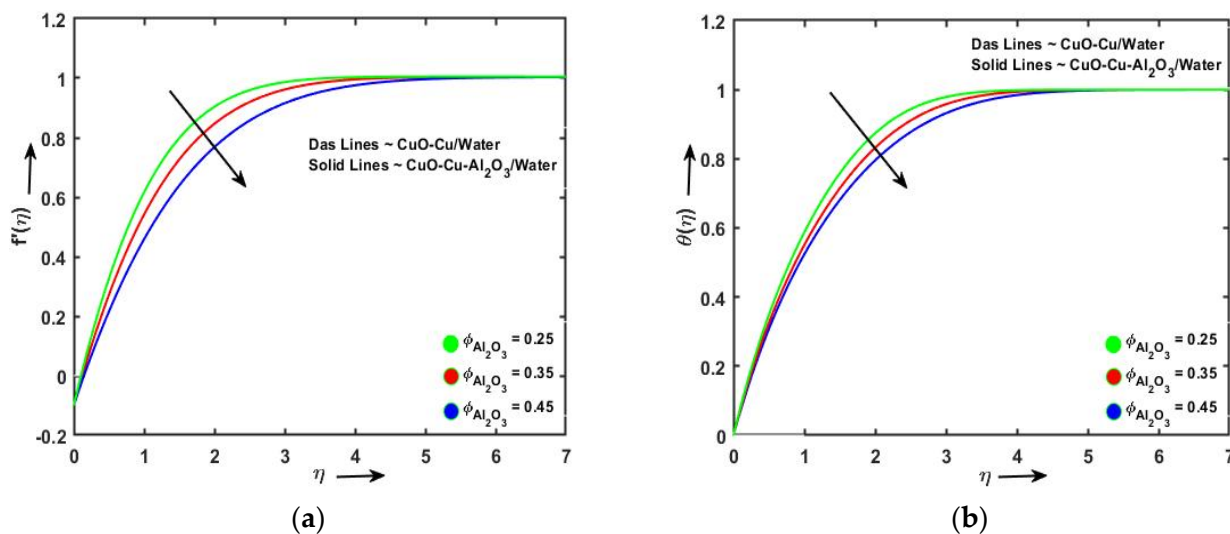


Figure 11. The (a) momentum and (b) temperature profiles of $\phi_{Al_2O_3}$.

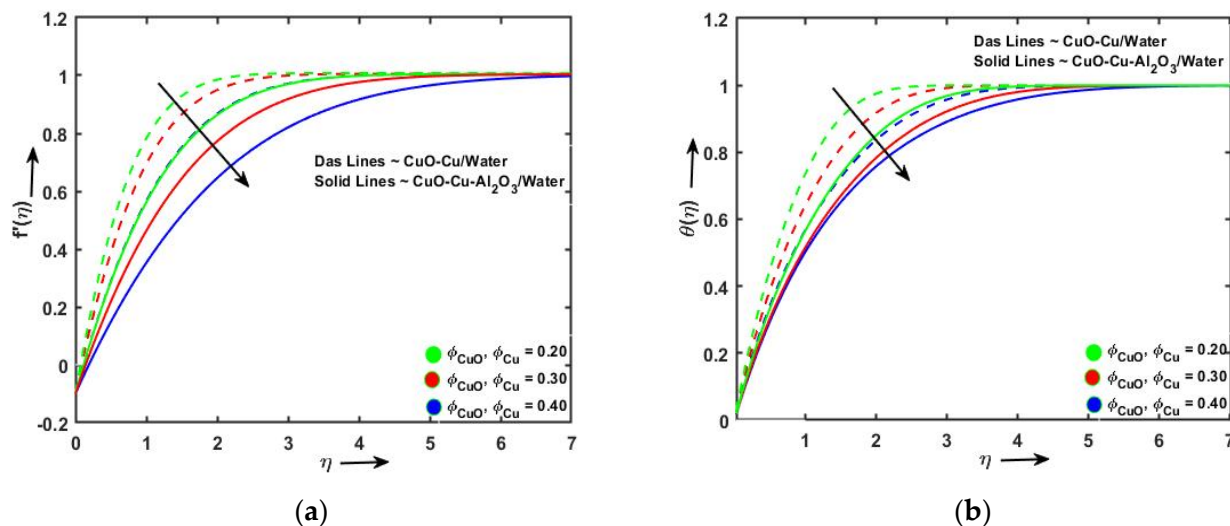


Figure 12. The (a) momentum and (b) temperature profiles of ϕ_{CuO} and ϕ_{Cu} .

Figure 5a,b illustrate the rising momentum and temperature outlines of the power law index, respectively. The increasing magnetic number declines to the velocity profile (Figure 6a) and grows to the temperature profile (Figure 6b). It is observed that the motion graphs reduce for more significant amounts of the magnetic field parameter. When we improve the magnetic field parameter, a resistive force named Lorentz force actively offers resistance against fluid particles; consequently, horizontal motion reduces. Thermal energy is released due to the additional effort required to pull the nanofluid against the magnetic field’s action. This warms the nanofluid, raises temperatures (Figure 6b), and thickens the thermal boundary layer for a sheet that is a shrinking sheet. Due to the growing melting effect, both velocity and temperature graphs fall off, as seen in Figure 7. It is also detected that the temperature reduces (Figure 7b), and the thermal boundary layer width improves for more significant values of the melting parameter. Physically, growth in the value of the melting parameter causes an upsurge in molecular movement, resulting in dissipation in energy and a decrease in the temperature of the fluid.

Table 4. The rates of skin-friction and Nusselt with Mn , G_T , α , n , W , δ_T and Ec when $Pr = 6.2$, $Me = 0.1$, $\lambda = -0.1$, $\phi_{CuO} = 0.20$, $\phi_{Cu} = 0.25$ and $\phi_{Al_2O_3} = 0.35$.

Mn	G_T	α	n	W	δ_T	Ec	CuO-Cu- Al_2O_3/H_2O		CuO-Cu/ H_2O		
							$C_{f_x}\sqrt{2Re_x}^{1/2}$	$Nu_x\sqrt{2Re_x}^{-1/2}$	$C_{f_x}\sqrt{2Re_x}^{1/2}$	$Nu_x\sqrt{2Re_x}^{-1/2}$	
0.1							8.927047972	-6.198828532	4.894402794	-3.813227424	
							11.143034493	-8.020221164	5.433157323	-4.288368467	
							13.383275047	-9.812182534	6.031744065	-4.809842051	
0.1	1.5						8.927047972	-6.198828532	4.893446770	-3.811927735	
							9.039911046	-6.286452677	4.993525133	-3.903802630	
0.5	1						9.184889066	-6.399489483	5.119261263	-4.020277174	
							$\pi/6$	8.934277295	-6.204740426	4.900228211	-3.818651672
							$\pi/4$	8.927047972	-6.198828532	4.894402794	-3.813227424
							$\pi/3$	8.917629262	-6.191131516	4.886812746	-3.806164135
1							8.927047972	-6.198828532	4.894402794	-3.813227424	
							0.1	8.949440436	-6.201321300	4.926321011	-3.817245819
							0.5	8.971965771	-6.203819563	4.958732360	-3.821286307
							0.9	8.927047972	-6.198828532	4.894402794	-3.813227424
							1	6.336483032	-5.819039998	2.683474467	-3.374176093
							2	4.222481257	-5.312300497	1.626149290	-2.969048910
							0.0005	-2.969048910	-6.198664878	4.894402756	-3.813102206
							0.0010	8.927047972			
							0.0015	8.927047703			
							0.1	8.927047972	-6.198828532	4.894402794	-3.813227424
0.5	8.833144216	-17.794316758	4.848093454	-9.939227882							
					0.7	8.787808564	-23.467557884	4.825687631	-12.942578233		

Figure 8a depicts the upsurge velocity profile for the thermal relaxation parameter. An upsurge temperature impression of the thermal relaxation, Eckert and Prandtl number is seen in Figures 8b and 9a,b, respectively. The temperature increases with thermal relaxation due to the thickness of the thermal boundary layer. The influence of the Eckert number on temperature outline is depicted in Figure 9a. It is noticed that the temperature profile is enhanced for positive values of the Eckert number. When the Eckert number increases, fluid particles are more dynamic and energetic; consequently, average kinetic energy rises, which yields an augmentation in liquid temperature. From the definition of the Prandtl number, it is explicit that greater Pr has a lesser thermal diffusivity. Due to the result of the melting parameter, the thermal boundary layer thickness increases by increasing Pr values and improves the thermal boundary layer width, as exposed in Figure 9b.

Figure 10a shows the decline momentum profile with the shrinking parameter. In the detail of Figure 10b, the temperature profile increases $\eta < 2.5$ with the modified nanofluid and $\eta < 0.7$ and the hybrid nanofluid. The temperature profile declines $\eta > 2.5$ with the modified nanofluid and $\eta > 0.7$ with the hybrid nanofluid. An increasing impression of volume-fraction of tiny particles falloffs to the velocity and temperature profiles for both modified and hybrid nanofluid (as shown in Figures 11 and 12). The effects of solid particles on the velocity field are shown in Figures 11a and 12a. The acceleration of the velocity profile is caused by the growth of solid nanoparticles in the modified nanofluid and hybrid nanofluid. The increased collision with suspended nanoparticles is what drives this phenomenon; and temperature declines due to the falling thermal boundary layer.

Table 5. The rates of skin-friction and Nusselt with Pr, Me, λ , ϕ_{CuO} , ϕ_{Cu} , and $\phi_{Al_2O_3}$ when Mn = Gr_T = n = W = δ_T = Ec = 0.1 and $\alpha = \pi/4$.

Pr	Me	λ	ϕ_{CuO}	ϕ_{Cu}	$\phi_{Al_2O_3}$	CuO-Cu-Al ₂ O ₃ /H ₂ O		CuO-Cu/H ₂ O	
						$C_{f_x} \sqrt{2Re_x}^{1/2}$	$Nu_x \sqrt{2Re_x}^{-1/2}$	$C_{f_x} \sqrt{2Re_x}^{1/2}$	$Nu_x \sqrt{2Re_x}^{-1/2}$
5.2						8.921092404	−5.561627924	4.890271980	−3.442597882
6.2						8.927047972	−6.198828532	4.894402794	−3.813227424
7.2						8.931869189	−6.805867799	4.897747610	−4.164290966
	0.1					8.927047972	−6.198828532	4.894402794	−3.813227424
	1					8.462962288	−5.372604369	4.616471710	−3.271921106
	2					8.080005569	−4.719097824	4.390985730	−2.851024087
		−0.1				8.927047972	−6.198828532	4.894402794	−3.813227424
		−0.4				10.188466357	−7.053427611	5.507954725	−4.116246768
		−0.7				10.766721071	−7.859191814	5.700393663	−4.309395629
			0.20			7.948470379	−5.660306008	4.297838195	−3.449087491
			0.30			12.479347624	−8.043118957	6.952368528	−5.004649610
			0.40			20.542630767	−11.787848721	11.479921474	−7.332749263
				0.25		7.396199827	−5.360729882		
				0.35		9.006005543	−6.207577317		
				0.45		11.361562610	−7.324523129		

Tables 4 and 5 show the flow and heat transfer rate of various non-dimensional parameters for both modified and hybrid nanofluid flows. The upsurge Grashof, power law index, and volume fractions of nanosized particles grow to the skin-friction coefficient. The skin-friction rate declines with the increasing acute angle, Weissenberg parameter, and melting impacts. The Nusselt number rises with the acute angle and melting impacts. A growing impression of the Grashof, power law index, thermal relaxation parameter, and volume fractions of tiny particles falloffs to the heat transfer rate.

6. Conclusions

This ground-breaking work explains the CuO – Cu-alumina/water-based Carreau-modified nanofluid flow with Cattaneo–Christov heat flux across an inclined moving shrinking sheet. It uses the bvp4c solver for the validation of the results. The synopsis of the conclusions drawn from this research are as follows:

- The velocity and temperature profiles decline with the rising Weissenberg parameter and inclined surface.
- The velocity declines with hybrid and modified nanofluid flow with the increasing volume fraction of nanoparticles.
- The motion and temperature grow with the upsurge power law index parameter.
- For hybrid and modified nanofluid flow, the power law index declines to heat transfer rate and grows to skin friction rate.
- The Nusselt number decreases with the upsurge thermal relaxation parameter in hybrid and modified nanofluid flow.
- An upsurge volume fraction of tiny particles reduces both velocity and temperature profiles.

Author Contributions: Conceptualization, S.J. and S.; methodology, S.J. and R.M.; software, S.J. and S.; validation, S.J.; formal analysis, N.A.; investigation, N.A.; resources, N.T.; data curation, N.T.; writing—original draft preparation, S.J.; writing—review and editing, N.A., N.T. and R.M.; visualization, N.T.; supervision, R.M.; project administration, N.A.; funding acquisition, N.A. All authors have read and agreed to the published version of the manuscript.

Funding: Princess Nourah Bint Abdulrahman University Researchers Supporting Project number (PNURSP2022R59), Princess Nourah Bint Abdulrahman University, Riyadh, Saudi Arabia.

Data Availability Statement: Not applicable.

Acknowledgments: Princess Nourah Bint Abdulrahman University Researchers Supporting Project number (PNURSP2022R59), Princess Nourah Bint Abdulrahman University, Riyadh, Saudi Arabia.

Conflicts of Interest: Not applicable.

Nomenclature

T_0	Solid surface temperature
T_m	Melting point temperature
T_∞	Free stream temperature
v	y -axis velocity
u	x -axis velocity
T	Fluid temperature
Γ	Time constant
B_0	Magnetic field strength
g	Gravitational acceleration
C_s	Solid surface specific heat
L	Latent heat
α	Acute angle
λ_T	Thermal relaxation constant
mnf	Modified nanofluid
$hbnf$	Hybrid nanofluid
Bf	Base fluid
ϕ_{CuO}	Volume fraction of CuO
ϕ_{Cu}	Volume fraction of Cu
$\phi_{Al_2O_3}$	Volume fraction of Al_2O_3
α_T	Thermal diffusivity
ρC_p	Heat capacity
C_p	Specific heat at constant pressure
σ	Electrical conductivity
β_T	Thermal expansion coefficient
k	Thermal conductivity
ρ	Density
μ	Dynamic viscosity
n	Power law index
η	Pseudo-similarity variable
f	Non-dimensional velocity parameter
θ	Non-dimensional temperature parameter
M	Shape factor
W	Local Weissenberg number
Mn	Hartmann parameter
G_T	Local Grashof temperature number
Pr	Prandtl number
δ_T	Thermal relaxation parameter
Ec	Eckert number
λ	Stretching/shrinking parameter
Me	Melting parameter
C_f	Skin friction

Nu_x	Nusselt number
τ_w	Surface shear stress
q_w	Heat transfer rate
Re_x	Reynolds number

References

- Lehmann, P.; Stauffer, F.; Hinz, C.; Dury, O.; Flüßler, H. Effect of hysteresis on water flow in a sand column with a fluctuating capillary fringe. *J. Contam. Hydrol.* **1998**, *33*, 81–100. [[CrossRef](#)]
- Waite, M.E.; Ge, S.; Spetzler, H. A new conceptual model for fluid flow in discrete fractures: An experimental and numerical study. *J. Geophys. Res. Solid Earth* **1999**, *104*, 13049–13059. [[CrossRef](#)]
- Bachok, N.; Ishak, A.; Pop, I. Melting heat transfer in boundary layer stagnation-point flow towards a stretching/shrinking sheet. *Phys. Lett. A* **2010**, *374*, 4075–4079. [[CrossRef](#)]
- Shigechi, T.; Davaa, G.; Momoki, S.; Jambal, O. Laminar heat transfer with viscous dissipation and fluid axial heat conduction for modified power law fluids flowing in parallel plates with one plate moving. *JSME Int. J. Ser. B Fluids Therm. Eng.* **2003**, *46*, 539–548. [[CrossRef](#)]
- Ellahi, R.; Riaz, A.; Nadeem, S.; Ali, M. Peristaltic flow of Carreau fluid in a rectangular duct through a porous medium. *Math. Probl. Eng.* **2012**, *2012*, 329639. [[CrossRef](#)]
- Salek, M.M.; Sattari, P.; Martinuzzi, R.J. Analysis of fluid flow and wall shear stress patterns inside partially filled agitated culture well plates. *Ann. Biomed. Eng.* **2012**, *40*, 707–728. [[CrossRef](#)] [[PubMed](#)]
- Hayat, T.; Asad, S.; Mustafa, M.; Alsaedi, A. Boundary layer flow of Carreau fluid over a convectively heated stretching sheet. *Appl. Math. Comput.* **2014**, *246*, 12–22. [[CrossRef](#)]
- Ahmad, S.; Pop, I. Melting effect on mixed convection boundary layer flow about a vertical surface embedded in a porous medium: Opposing flows case. *Transp. Porous Media* **2014**, *102*, 317–323. [[CrossRef](#)]
- Mustafa, M. Cattaneo-Christov heat flux model for rotating flow and heat transfer of upper-convected Maxwell fluid. *Aip Adv.* **2015**, *5*, 47109. [[CrossRef](#)]
- Han, S.; Zheng, L.; Li, C.; Zhang, X. Coupled flow and heat transfer in viscoelastic fluid with Cattaneo–Christov heat flux model. *Appl. Math. Lett.* **2014**, *38*, 87–93. [[CrossRef](#)]
- Malvandi, A.; Moshizi, S.A.; Soltani, E.G.; Ganji, D.D. Modified Buongiorno’s model for fully developed mixed convection flow of nanofluids in a vertical annular pipe. *Comput. Fluids* **2014**, *89*, 124–132. [[CrossRef](#)]
- Akbar, N.S.; Nadeem, S. Carreau fluid model for blood flow through a tapered artery with a stenosis. *Ain Shams Eng. J.* **2014**, *5*, 1307–1316. [[CrossRef](#)]
- Pantokratoras, A. Non-similar Blasius and Sakiadis flow of a non-Newtonian Carreau fluid. *J. Taiwan Inst. Chem. Eng.* **2015**, *56*, 1–5. [[CrossRef](#)]
- Akbar, N.S.; Ebaid, A.; Khan, Z.H. Numerical analysis of magnetic field effects on Eyring-Powell fluid flow towards a stretching sheet. *J. Magn. Magn. Mater.* **2015**, *382*, 355–358. [[CrossRef](#)]
- Khan, M. Boundary layer flow and heat transfer to Carreau fluid over a nonlinear stretching sheet. *AIP Adv.* **2015**, *5*, 107203. [[CrossRef](#)]
- Khan, M.; Hussain, M.; Azam, M. Magnetohydrodynamic flow of Carreau fluid over a convectively heated surface in the presence of non-linear radiation. *J. Magn. Magn. Mater.* **2016**, *412*, 63–68. [[CrossRef](#)]
- Hayat, T.; Khan, M.I.; Farooq, M.; Alsaedi, A.; Waqas, M.; Yasmeen, T. Impact of Cattaneo–Christov heat flux model in flow of variable thermal conductivity fluid over a variable thicked surface. *Int. J. Heat Mass Transf.* **2016**, *99*, 702–710. [[CrossRef](#)]
- Akbari, O.A.; Safaei, M.R.; Goodarzi, M.; Akbar, N.S.; Zarringhalam, M.; Shabani, G.A.S.; Dahari, M. A modified two-phase mixture model of nanofluid flow and heat transfer in a 3-D curved microtube. *Adv. Powder Technol.* **2016**, *27*, 2175–2185. [[CrossRef](#)]
- Animasaun, I.L. Double diffusive unsteady convective micropolar flow past a vertical porous plate moving through binary mixture using modified Boussinesq approximation. *Ain Shams Eng. J.* **2016**, *7*, 755–765. [[CrossRef](#)]
- Khan, M.; Irfan, M.; Khan, W.A.; Alshomrani, A.S. A new modeling for 3D Carreau fluid flow considering nonlinear thermal radiation. *Results Phys.* **2017**, *7*, 2692–2704. [[CrossRef](#)]
- Khan, M.; Malik, M.Y.; Salahuddin, T.; Khan, I. Numerical modeling of Carreau fluid due to variable thicked surface. *Results Phys.* **2017**, *7*, 2384–2390. [[CrossRef](#)]
- Devi, S.S.U.; Devi, S.P.A. Heat transfer enhancement of Cu-Al₂O₃/water hybrid nanofluid flow over a stretching sheet. *Alex. Eng. J.* **2017**, *36*, 419–433.
- Khan, M. On Cattaneo-Christov heat flux model for Carreau fluid flow over a slendering sheet. *Results Phys.* **2017**, *7*, 310–319.
- Khan, M.; Sardar, H.; Gulzar, M.M.; Saleh, A. On multiple solutions of non-Newtonian Carreau fluid flow over an inclined shrinking sheet. *Results Phys.* **2018**, *8*, 926–932. [[CrossRef](#)]
- Sharma, R.P.; Makinde, O.D.; Animasaun, I.L. Buoyancy effects on MHD unsteady convection of a radiating chemically reacting fluid past a moving porous vertical plate in a binary mixture. In *Defect and Diffusion Forum*; Trans Tech Publications Ltd.: Bäch, Switzerland, 2018; Volume 387, pp. 308–318.
- Mumraiz, S.; Ali, A.; Meshal, M.A.; Zahir, S. Entropy generation in electrical magnetohydrodynamic flow of Al₂O₃-Cu/H₂O hybrid nanofluid with non-uniform heat flux. *J. Therm. Anal. Calorim.* **2020**, *143*, 2135–2148. [[CrossRef](#)]

27. Ali, A.; Sana, S.S.; Anber, M.; Marwat, D.N.K. Investigation on $\text{TiO}_2\text{-Cu}/\text{H}_2\text{O}$ hybrid nanofluid with slip conditions in MHD peristaltic flow of Jeffrey material. *J. Therm. Anal. Calorim.* **2021**, *143*, 1985–1996. [[CrossRef](#)]
28. Abbasi, A.; Al-Khaled, K.; Khad, M.I.; Khan, S.U.; El-Refaey, A.M.; Farooq, W.; Jameel, M.; Qayyum, S. Optimized analysis and enhanced thermal efficiency of modified hybrid nanofluid (Al_2O_3 , CuO, Cu) with nonlinear thermal radiation and shape features. *Case Stud. Therm. Eng.* **2021**, *28*, 101425. [[CrossRef](#)]
29. Khan, M.; Hussain, A.; Malik, M.Y.; Salahuddin, T.; Aly, S. Numerical analysis of Carreau fluid flow for generalized Fourier's and Fick's laws. *Appl. Numer. Math.* **2019**, *144*, 100–117. [[CrossRef](#)]
30. Madhu, M.; Mahanthesh, B.; Shashikumar, N.S.; Shehzad, S.A.; Khan, S.U.; Gireesha, B.J. Performance of second law in Carreau fluid flow by an inclined microchannel with radiative heated convective condition. *Int. Commun. Heat Mass Transf.* **2020**, *117*, 104761. [[CrossRef](#)]
31. Loganathan, K.; Sivasankaran, S.; Bhuvaneshwari, M.; Rajan, S. Second-order slip, cross-diffusion and chemical reaction effects on magneto-convection of Oldroyd-B liquid using Cattaneo–Christov heat flux with convective heating. *J. Therm. Anal. Calorim.* **2019**, *136*, 401–409. [[CrossRef](#)]
32. Abbas, N.; Nadeem, S.; Saleem, A.; Malik, M.Y.; Issakhov, A.; Alharabi, F.M. Models base study of inclined MHD of hybrid nanofluid flow over nonlinear stretching cylinder. *Chinese J. Phys.* **2021**, *69*, 109–117. [[CrossRef](#)]
33. Khan, M.; Rasheed, A. Slip velocity and temperature jump effects on molybdenum disulfide MoS_2 and silicon oxide SiO_2 hybrid nanofluid near irregular 3D surface. *Alexandria Eng. J.* **2021**, *60*, 1689–1701. [[CrossRef](#)]
34. Jumana, S.A.; Murtaza, M.G.; Ferdows, M.; Makinde, O.D.; Zaimi, K. Dual solutions analysis of melting phenomenon with mixed convection in a nanofluid flow and heat transfer past a permeable stretching/shrinking sheet. *J. Nanofluids* **2020**, *9*, 313–320. [[CrossRef](#)]
35. Anwar, T.; Kumam, P.; Thounthong, P. Fractional Modeling and Exact Solutions to Analyze Thermal Performance of $\text{Fe}_3\text{O}_4\text{-MoS}_2\text{-Water}$ Hybrid Nanofluid Flow Over an Inclined Surface With Ramped Heating and Ramped Boundary Motion. *IEEE Access* **2021**, *9*, 12389–12404. [[CrossRef](#)]
36. Khan, W.U.; Awais, M.; Parveen, N.; Ali, A.; Awan, S.E.; Malik, M.Y.; He, Y. Analytical Assessment of ($\text{Al}_2\text{O}_3\text{-Ag}/\text{H}_2\text{O}$) Hybrid Nanofluid Influenced by Induced Magnetic Field for Second Law Analysis with Mixed Convection, Viscous Dissipation and Heat Generation. *Coatings* **2021**, *11*, 498. [[CrossRef](#)]
37. Ali, A.; Kanwal, T.; Awais, M.; Shah, Z.; Kumam, P.; Thounthong, P. Impact of thermal radiation and non-uniform heat flux on MHD hybrid nanofluid along a stretching cylinder. *Sci. Rep.* **2021**, *11*, 20262. [[CrossRef](#)]
38. Zhang, Y.; Shahmir, N.; Ramzan, M.; Ghazwani, H.A.S.; Malik, M.Y. Comparative analysis of Maxwell and Xue models for a hybrid nanofluid film flow on an inclined moving substrate. *Case Stud. Therm. Eng.* **2021**, *28*, 101598. [[CrossRef](#)]
39. Alzahrani, A.K.; Ullah, M.Z.; Alshomrani, A.S.; Gul, T. Hybrid nanofluid flow in a Darcy-Forchheimer permeable medium over a flat plate due to solar radiation. *Case Stud. Therm. Eng.* **2021**, *26*, 100955. [[CrossRef](#)]
40. Abbas, N.; Nadeem, S.; Issakhov, A. Transportation of modified nanofluid flow with time dependent viscosity over a Riga plate: Exponentially stretching. *Ain Shams Eng. J.* **2021**, *12*, 3967–3973. [[CrossRef](#)]
41. Ahmad, I.; Faisal, M.; Zan-Ul-Abadin, Q.; Javed, T.; Loganathan, K. Unsteady 3D heat transport in hybrid nanofluid containing brick shaped ceria and zinc-oxide nanocomposites with heat source/sink. *Nanocomposites* **2022**, *8*, 1–12. [[CrossRef](#)]
42. Eswaramoorthi, S.; Loganathan, K.; Jain, R.; Gyeltshen, S. Darcy-Forchheimer 3D Flow of Glycerin-Based Carbon Nanotubes on a Riga Plate with Nonlinear Thermal Radiation and Cattaneo-Christov Heat Flux. *J. Nanomater.* **2022**, *2022*, 5286921. [[CrossRef](#)]
43. Gowda, R.J.P.; Al-Mubaddel, F.S.; Kumar, R.N.; Prasannakumara, B.C.; Issakhov, A.; Rahimi-Gorji, M.; Al-Turki, Y.A. Computational modelling of nanofluid flow over a curved stretching sheet using Koo–Kleinstreuer and Li (KKL) correlation and modified Fourier heat flux model. *Chaos Solitons Fractals* **2021**, *145*, 110774. [[CrossRef](#)]
44. Ramzan, M.; Gul, H.; Mursaleen, M.; Nisar, K.S.; Jamshed, W.; Muhammad, T. Von Karman rotating nanofluid flow with modified Fourier law and variable characteristics in liquid and gas scenarios. *Sci. Rep.* **2021**, *11*, 16442. [[CrossRef](#)]
45. Reddy, P.S.; Sreedevi, P. Flow and heat transfer analysis of carbon nanotubes based nanofluid flow inside a cavity with modified Fourier heat flux. *Phys. Scr.* **2021**, *96*, 55215. [[CrossRef](#)]
46. Ali, F.; Loganathan, K.; Eswaramoorthi, S.; Prabu, K.; Zaib, A.; Chaudhary, D.K. Heat Transfer Analysis on Carboxymethyl Cellulose Water-Based Cross Hybrid Nanofluid Flow with Entropy Generation. *J. Nanomater.* **2022**, *2022*, 5252918. [[CrossRef](#)]
47. Prabakaran, R.; Eswaramoorthi, S.; Loganathan, K.; Sarris, I.E. Investigation on Thermally Radiative Mixed Convective Flow of Carbon Nanotubes/ Al_2O_3 Nanofluid in Water Past a Stretching Plate with Joule Heating and Viscous Dissipation. *Micromachines* **2022**, *13*, 1424. [[CrossRef](#)] [[PubMed](#)]
48. Kiyani, M.Z.; Hayat, T.; Ahmad, I.; Waqas, M.; Alsaedi, A. Bidirectional Williamson nanofluid flow towards stretchable surface with modified Darcy's law. *Surf. Interfaces* **2021**, *23*, 100872. [[CrossRef](#)]
49. Syahirah, N.; Arifin, N.; Pop, I.; Bachok, N. MHD stagnation-point flow of nanofluid due to a shrinking sheet with melting, viscous dissipation and Joule heating effects. *Alexandria Eng. J.* **2022**, *61*, 12661–12672. [[CrossRef](#)]
50. Anwar, T.; Kumam, P.; Thounthong, P. A comparative fractional study to evaluate thermal performance of $\text{NaAlG-MoS}_2\text{-Co}$ hybrid nanofluid subject to shape factor and dual ramped conditions. *Alexandria Eng. J.* **2022**, *61*, 2166–2187. [[CrossRef](#)]
51. Ali, A.; Sajid, M.; Anjum, H.J.; Awais, M.; Nisar, K.S.; Saleel, C.A. Entropy Generation Analysis of Peristaltic Flow of Nanomaterial in a Rotating Medium through Generalized Compliant Walls of Micro-Channel with Radiation and Heat Flux Effects. *Micromachines* **2022**, *13*, 375. [[CrossRef](#)]